

Rho GTPase complementation underlies BDNF-dependent homo- and heterosynaptic plasticity

Nathan G. Hedrick^{1*†}, Stephen C. Harward^{1*}, Charles E. Hall¹, Hideji Murakoshi², James O. McNamara¹ & Ryohei Yasuda^{1,3}

The Rho GTPase proteins Rac1, RhoA and Cdc42 have a central role in regulating the actin cytoskeleton in dendritic spines¹, thereby exerting control over the structural and functional plasticity of spines^{2–5} and, ultimately, learning and memory^{6–8}. Although previous work has shown that precise spatiotemporal coordination of these GTPases is crucial for some forms of cell morphogenesis⁹, the nature of such coordination during structural spine plasticity is unclear. Here we describe a three-molecule model of structural long-term potentiation (sLTP) of murine dendritic spines, implicating the localized, coincident activation of Rac1, RhoA and Cdc42 as a causal signal of sLTP. This model posits that complete tripartite signal overlap in spines confers sLTP, but that partial overlap primes spines for structural plasticity. By monitoring the spatiotemporal activation patterns of these GTPases during sLTP, we find that such spatiotemporal complementation simultaneously explains three integral features of plasticity: the facilitation of plasticity by brain-derived neurotrophic factor (BDNF), the postsynaptic source of which activates Cdc42 and Rac1, but not RhoA; heterosynaptic facilitation of sLTP, which is conveyed by diffusive Rac1 and RhoA activity; and input specificity, which is afforded by spine-restricted Cdc42 activity. Thus, we present a form of biochemical computation

in dendrites involving the controlled complementation of three molecules that simultaneously ensures signal specificity and primes the system for plasticity.

Previous studies using two-photon fluorescence lifetime imaging (2pFLIM) in combination with fluorescence resonance energy transfer (FRET)-based biosensors revealed that the Rho GTPases Cdc42 and RhoA had distinct spatial profiles during sLTP, with Cdc42 showing synapse-restricted activity and RhoA showing a diffuse, heterosynaptic pattern³. To obtain a more complete understanding of the spatiotemporal patterning of Rho GTPase activity during sLTP, we developed a FRET-based sensor for Rac1, following the design of the Cdc42 and RhoA sensors³ (Fig. 1a; validation in Extended Data Figs 1–3). We transfected rat organotypic hippocampal slices with the sensor using biolistics^{10,11} and imaged CA1 pyramidal neurons using 2pFLIM¹². When sLTP was induced in single dendritic spines with two-photon glutamate uncaging^{13,14} (Fig. 1b, c), Rac1 was rapidly (within ~1 min) activated in the stimulated spine, and remained active for at least 30 min (Fig. 1b, d), notably displaying a more pronounced sustained phase than RhoA or Cdc42 (ref. 3). This activation initially showed limited diffusion, after which it slowly spread over ~10 μm of the parent dendrite until it nearly equalized with activity

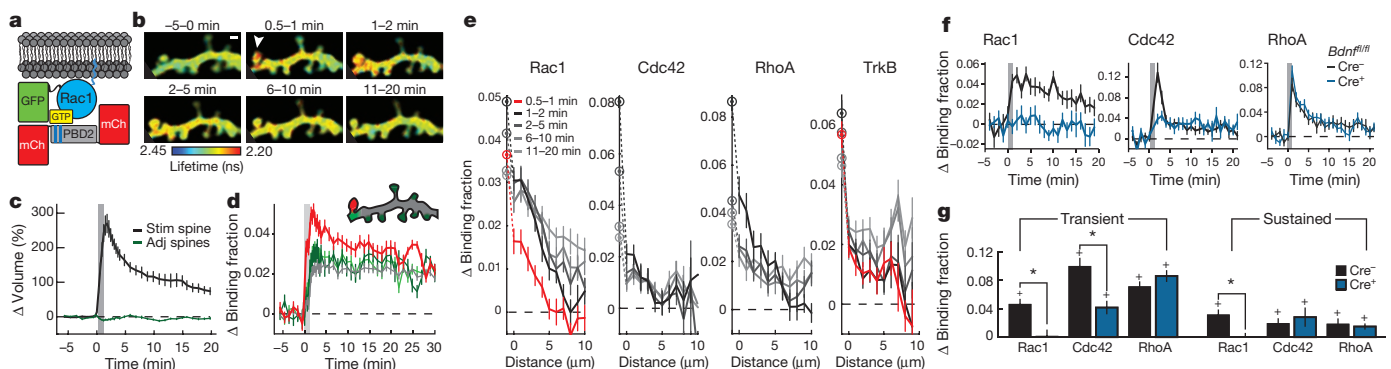


Figure 1 | The Rho GTPases Rac1 and Cdc42 convey postsynaptic BDNF-TrkB signalling across both homosynaptic and heterosynaptic domains.

a, Schematic of Rac1 sensor. Monomeric enhanced green fluorescent protein (eGFP) is N-terminally tagged to Rac1 to preserve C-terminal membrane association. GTP binding leads to association with the Pak GTPase binding domain of $\text{PAK}2^{\text{R71C,S78A}}$ (PBD2; blue lines denote mutations), bringing the mCherry (mCh) fluorophores within the FRET distance of eGFP, decreasing its fluorescence lifetime. **b**, Representative 2pFLIM images of Rac1 activation in dendrites during sLTP induced in a single spine with two-photon glutamate uncaging (white arrowhead). Scale bar, 1 μm . **c**, Time course of spine volume changes during sLTP induced with two-photon glutamate uncaging (grey window) in the stimulated spine (black) and compared to adjacent spines (green). $n = 102$ cells/121 spines. **d**, Time course of Rac1 activation during sLTP, measured as a change in the fraction of acceptor-bound eGFP-Rac1

in the stimulated spine (black), nearby spines (green), dendrite near the stimulated spine (cyan) and whole dendrite in the image (grey). $n = 102/121$ (cells/spines). **e**, Activations of Rac1 ($n = 56/79$), Cdc42 ($n = 25/38$), RhoA ($n = 21/23$), and TrkB ($n = 48/52$) (cells/spines) in dendrites as a function of distances from the base of the stimulated spines (lines) and in the stimulated spines (circles). **f**, Dependence of Rho GTPase activation on postsynaptically synthesized BDNF. Blue indicates co-expression of Cre recombinase in $\text{Bdnf}^{\text{fl/fl}}$ slices along with the Rac1 (left; $n = 7/13$ Cre⁻, $n = 8/16$ Cre⁺), Cdc42 (middle; $n = 5/12$ Cre⁻, $n = 4/11$ Cre⁺), or RhoA (right; $n = 6/13$ Cre⁻, $n = 7/14$ Cre⁺) (cells/spines) sensor. Black represents the corresponding control (Cre⁻) data. **g**, Summary of data from **f**. Bars represent the average of the activation 1–2 min after stimulation. Error bars represent s.e.m. * $P < 0.05$ (two-tailed t -test between groups); + $P < 0.05$ (t -test compared to the baseline).

¹Neurobiology Department, Duke University Medical Center, Research Drive, Durham, North Carolina 27710, USA. ²National Institute for Physiological Science, Myodaiji, Okazaki, Aichi, 444-8585, Japan. ³Max Planck Florida Institute for Neuroscience, 1 Max Planck Way, Jupiter, Florida 33458, USA. [†]Present address: Neurobiology Section, Center for Neural Circuits and Behavior, and Department of Neurosciences, University of California, San Diego, 9500 Gilman Drive, La Jolla, California 92093, USA.

*These authors contributed equally to this work.

in the spine (Fig. 1b, d, e, Extended Data Fig. 2a, b). Similar to Cdc42 and RhoA, Rac1 activation was dependent on NMDARs (*N*-methyl-D-aspartate receptors) and CaMKII (Extended Data Fig. 2d–f), and both pharmacological inhibition of Rac1 and single-cell knockout of Rac1 inhibited sLTP (Extended Data Fig. 4). Thus, like RhoA and Cdc42, Rac1 is a Rho GTPase molecule linking NMDAR–CaMKII signalling to sLTP.

We next examined whether postsynaptic BDNF¹⁵, which also links NMDAR–CaMKII signalling and sLTP, is required for Rho GTPase activation during sLTP. To do this, we used a single-cell knockout technique^{15,16} with organotypic hippocampal slices from BDNF conditional knockout mice (*Bdnf^{fl/fl}*)^{17,36} coupled with biolistic transfection of Cre recombinase alongside a Rho GTPase sensor. We found that removal of postsynaptic BDNF significantly attenuated Rac1 and Cdc42 activation during sLTP without affecting RhoA (Fig. 1f, g), and reduced the associated expression of sLTP¹⁵ (Extended Data Fig. 5a, b). This suggests that Rac1 and Cdc42, but not RhoA, are downstream of postsynaptic BDNF. Similarly, addition of the extracellular BDNF scavenger TrkB-Ig (2 $\mu\text{g ml}^{-1}$) significantly attenuated the activation of both Rac1 and Cdc42 (Extended Data Fig. 5c, d, g, h). Finally, postsynaptic removal of the BDNF receptor TrkB using *Trkb^{fl/fl}* (also known as *Ntrk2^{fl/fl}*) mice also significantly attenuated Rac1 and Cdc42 activation (Extended Data Fig. 5e, f, i, j). These results suggest that an autocrine BDNF–TrkB system controls the activation of Rac1 and Cdc42, thereby instructing two distinct spatial signalling domains relevant to plasticity: a spine-specific domain comprising BDNF–TrkB–Cdc42, and a diffuse domain comprising BDNF–TrkB–Rac1. Since BDNF–TrkB signalling is preferentially enriched in stimulated spines during sLTP (Fig. 1e, Extended Data Fig. 2a),

diffusion of Rac1 molecules (Extended Data Fig. 2c) or of Rac1 activators downstream of TrkB^{7,18} probably caused the observed spreading of Rac1 activity. By contrast, the spatial spreading of Cdc42 (before its decay) was similar to that of TrkB during the same time period (Extended Data Fig. 2b).

Notably, the length scale of Rac1 spreading is similar to that of synaptic crosstalk, a phenomenon in which sLTP induction briefly facilitates sLTP in nearby (~ 5 – $10 \mu\text{m}$) spines on the same dendrite^{19,20}. Thus, we next addressed whether BDNF–TrkB–Rac1 signalling contributes to such crosstalk. Consistent with previous studies^{19,20}, a suprathreshold sLTP stimulus delivered to one spine allowed a subsequent subthreshold stimulus at a nearby ($\leq 5 \mu\text{m}$) spine to induce sLTP (hereafter referred to as crosstalk) (Fig. 2a, b). To test whether crosstalk requires BDNF–TrkB–Rac1 signalling, we first used partial pharmacological inhibition of this pathway. Although strong inhibition of BDNF signalling has been shown to impair sLTP¹⁵, we found that weak inhibition of this pathway with a low concentration (0.25 $\mu\text{g ml}^{-1}$) of TrkB-Ig preserved sLTP ($\Delta V_{\text{supra sustained}} = 58 \pm 13\%$ (mean \pm s.e.m.), in which V denotes spine volume), but attenuated crosstalk ($\Delta V_{\text{sub sustained}} = 20 \pm 8\%$), suggesting that BDNF is required for this process (Fig. 2c, g). To ensure that these effects were due to BDNF signalling through TrkB, we used *Trkb^{F616A}* mutant mice, which contain a point mutation that renders TrkB uniquely susceptible to inhibition by the small molecule 1NMPP1 (ref. 21). We found that application of a low concentration (0.125 μM) of 1NMPP1 in *Trkb^{F616A}* slices selectively abolished crosstalk without affecting sLTP ($\Delta V_{\text{supra sustained}} = 59 \pm 16\%$, $\Delta V_{\text{sub sustained}} = 9 \pm 8\%$) (Fig. 2d, g). Interestingly, weak BDNF–TrkB inhibition also reduced Rac1 activity in dendritic shafts during the time frame of crosstalk induction (1–2 min), without inhibiting the activity

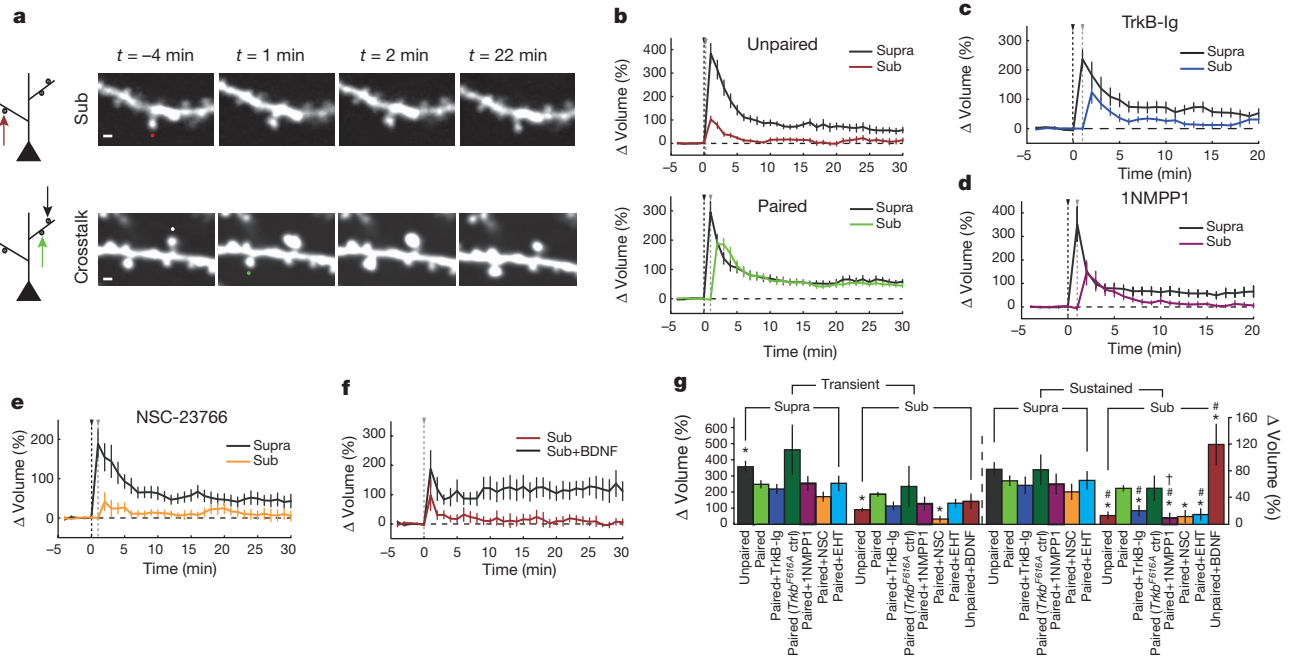


Figure 2 | BDNF–TrkB–Rac1 signalling is required for synaptic crosstalk. **a**, Left, schematic of crosstalk model. Top, in ‘unpaired’ trials, the subthreshold (sub) stimulus was delivered to a single spine. Bottom, in the ‘paired’ (crosstalk) condition, a threshold stimulus was delivered to a spine before the delivery of a subthreshold stimulus to a nearby spine on the same dendrite. Right, representative images of unpaired (top) and paired (bottom) subthreshold stimuli. Scale bars, 1 μm . **b**, Quantification of volume change for unpaired (top; $n = 24/27$ suprathreshold (supra), $n = 25/29$ sub) (cells/spines) and paired (bottom; $n = 35/47$) (cells/spine pairs) stimuli. Black and grey triangles indicate suprathreshold and subthreshold stimuli, respectively. **c**, Effect of 0.25 $\mu\text{g ml}^{-1}$ TrkB-Ig on synaptic crosstalk. $n = 6/13$ (cells/spine pairs). **d**, Effect of 0.125 μM 1NMPP1 on synaptic crosstalk in *Trkb^{F616A}* mice. $n = 5/10$ (cells/spine

pairs). **e**, Effect of the Rac1 inhibitor NSC-23766 (NSC; 15 μM) on synaptic crosstalk. $n = 6/10$ (cells/spine pairs). **f**, Effect of 20 ng ml^{-1} BDNF on spine volume change after a subthreshold stimulus. $n = 6/6$ sub, $n = 6/7$ sub plus BDNF. **g**, Summary of **b–f**, with the addition of the Rac1 inhibitor EHT-1864 (EHT; $n = 7/12$; cells/spine pairs) and *Trkb^{F616A}* cells in the absence of 1NMPP1 (*Trkb^{F616A}* ctrl; $n = 5/7$; cells/spine pairs) showing averages of transient (1–2 min after stimulation) and sustained (>10 min after stimulation) phases of sLTP. Left, spines stimulated with a threshold stimulus. Right, spines stimulated with an unpaired or paired subthreshold stimulus. * $P < 0.05$ (Dunnett’s test, versus the ‘paired’ subthreshold stimulus standard the crosstalk ‘control’); # $P < 0.05$ (two-tailed *t*-test, versus each condition’s paired crosstalk control).

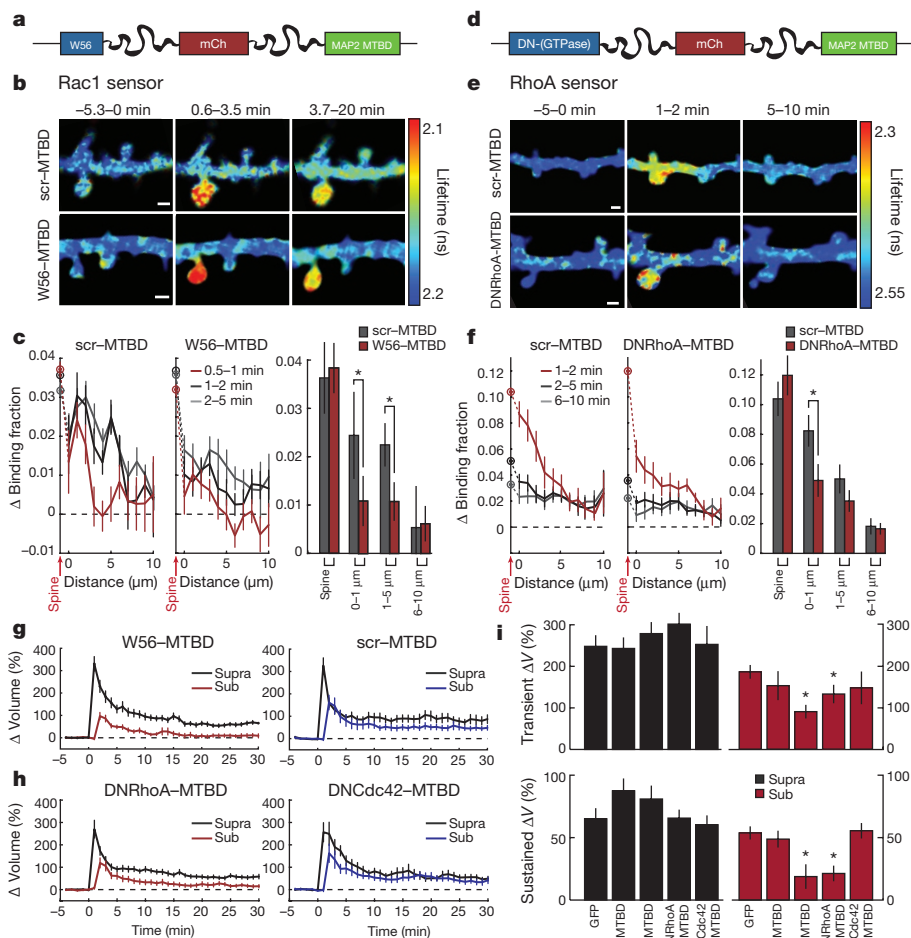


Figure 3 | Inhibition of signal spreading of Rac1 and RhoA prevents synaptic crosstalk. **a**, Schematic of the dendritic Rac1 inhibitor construct. W56 is fused to mCh and the microtubule binding domain (MTBD) of human MAP2 via intermediate linker sequences (wavy lines). **b**, Representative 2pFLIM images of the effect of W56-mCh-MTBD (W56-MTBD; bottom) or scrambled control (scr-MTBD; top) on the activation profile of the Rac1 sensor. Scale bars, 1 μm . **c**, Quantification of the spreading of Rac1 in scrambled control (left; $n = 10/17$) versus W56-mCh-MTBD (middle; $n = 22/36$) (cells/dendrite). Data represent the change in binding fraction in the dendrite as a function of distance from the stimulated spine (lines) and in the stimulated spines (circles) in the indicated time epochs. Right, Rac1 signal spreading in the presence of W56-mCh-MTBD across the indicated spatial windows at 1–2 min after stimulation. * $P < 0.05$, two-tailed t -test. **d**, Schematic of the dendritic

in the stimulated spines (Extended Data Fig. 6d–g). Likewise, while a high concentration of the Rac1 inhibitor NSC-23766 significantly reduced sLTP (Extended Data Fig. 4a, c), a small concentration (15 μM) inhibited crosstalk without significantly affecting sLTP ($\Delta V_{\text{supra sustained}} = 48 \pm 12\%$, $\Delta V_{\text{sub sustained}} = 12 \pm 10\%$) (Fig. 2e, g). This NSC-23766 concentration also trended towards decreasing the Rac1 activation in the shaft (Extended Data Fig. 6h, i). These data suggest that BDNF initiates a signalling cascade capable of lowering the threshold of structural plasticity, consistent with previous reports implicating BDNF in similar phenomena²². Indeed, exogenous BDNF (20 ng ml⁻¹) application for ~10–15 min allowed a subthreshold stimulus alone to induce sLTP ($\Delta V_{\text{sub sustained}} = 119 \pm 31\%$) (Fig. 2f, g). Notably, BDNF application alone was sufficient to activate Rac1 and Cdc42, but had no significant effect on spine volume (Extended Data Fig. 7), suggesting that BDNF is facilitative of, but insufficient for, sLTP. Taken together, these results suggest that the BDNF–TrkB–Rac1 signalling initiated in a single spine during sLTP induction facilitates sLTP in nearby spines, allowing synaptic crosstalk.

RhoA inhibitor, dominant-negative (DN) RhoA-mCh-MTBD. **e**, Representative 2pFLIM images of the effect of DNRhoA-mCh-MTBD expression on the activation profile of the RhoA sensor (bottom) versus scrambled control (top). Scale bars, 1 μm . **f**, Quantification of the spreading of RhoA in control ($n = 8/17$) versus DNRhoA-mCh-MTBD ($n = 11/18$) (cells/dendrite). Right, summary of RhoA spreading data. * $P < 0.05$, two-tailed t -test. **g**, Effect of W56-mCh-MTBD (left; $n = 30/47$) versus scr-mCh-MTBD (right; $n = 14/17$) (cells/spine pairs) expression on synaptic crosstalk. **h**, Effect of DNRhoA-mCh-MTBD (left; $n = 14/26$) and DNCdc42-mCh-MTBD (right; $n = 10/15$) (cells/spine pairs) on synaptic crosstalk. **i**, Summary of crosstalk experiments. Right, averages for the crosstalk spine. Left, averages of the first ('LTP') spine. * $P < 0.05$, Dunnett's test, compared to eGFP control.

To probe the requirement of heterosynaptic Rac1 activity for synaptic crosstalk more specifically, we devised a strategy to interrupt Rac1 activity spreading out of the stimulated spine during sLTP: we restricted the Rac1 inhibitory peptide W56 (ref. 23) to dendrites by fusing it to the microtubule binding domain (MTBD) of MAP2, concentrating the inhibitor to dendritically enriched microtubules^{24,25} (Fig. 3a, Extended Data Fig. 8a). This construct, W56-mCh-MTBD (in which mCh denotes mCherry), was concentrated in dendritic shafts and excluded from spines (Extended Data Fig. 8a). We found that this inhibitor significantly reduced Rac1 activation in the dendritic shaft, while largely preserving its activation in the stimulated spine (Fig. 3b, c). By contrast, W56-mCh without MTBD resulted in a more global reduction in Rac1 activation (Extended Data Fig. 8c, d). When the W56 peptide was scrambled (scr-mCh-MTBD), Rac1 activity spreading was normal (Fig. 3b, c). Finally, W56-mCh-MTBD did not change the spatial spreading of RhoA (Extended Data Fig. 8e). These results suggest that W56-mCh-MTBD specifically inhibits the spreading of Rac1 activity into dendrites.

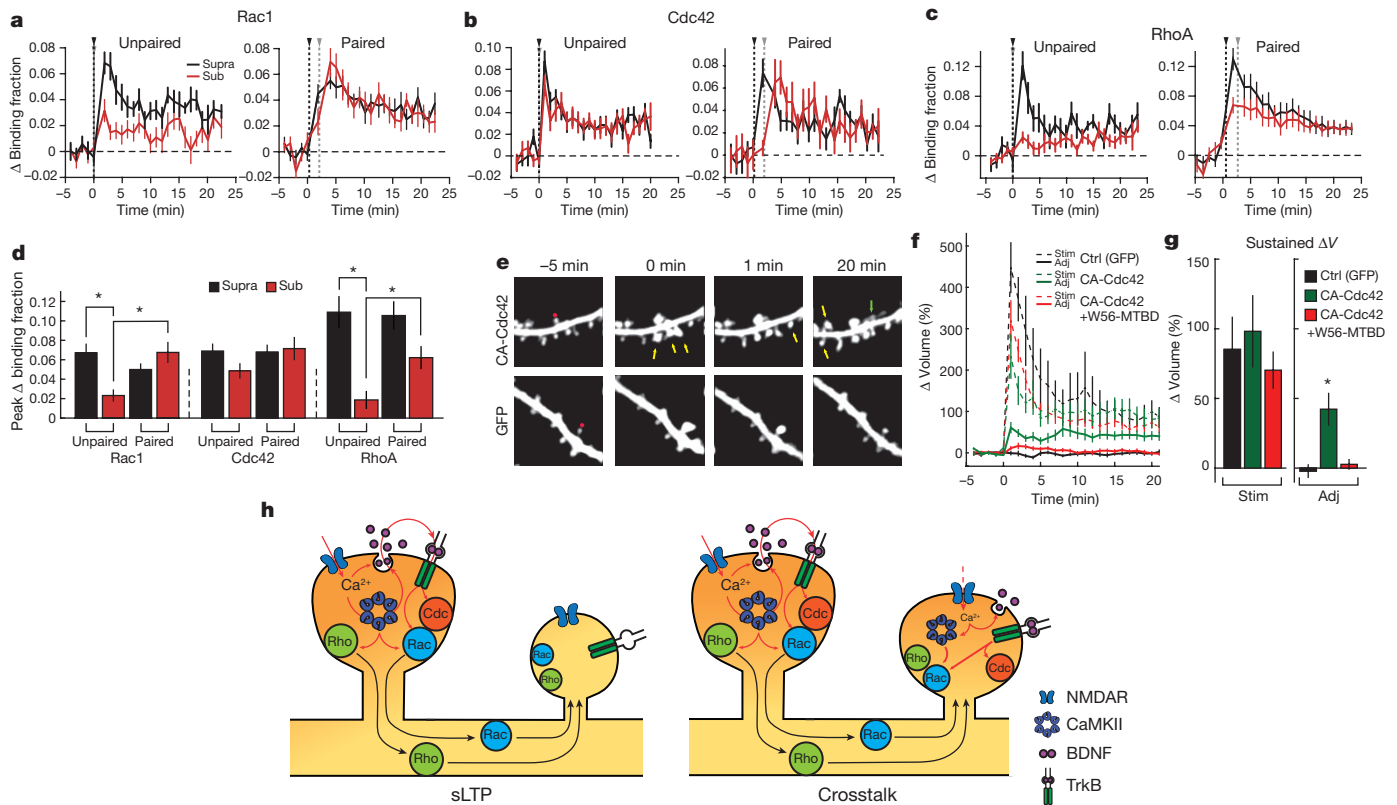


Figure 4 | Signal spreading provides additive activation of high-threshold signals during synaptic crosstalk. **a**, Comparison of Rac1 activation in response to unpaired (left; suprathreshold (black) $n = 12/12$, subthreshold (red) $n = 15/15$; cells/spines) and paired crosstalk (right; $n = 5/9$; cells/spine pairs) stimuli. Black and grey arrows indicate supra/subthreshold stimulus onset. **b**, Same as **a** for Cdc42 activity (left: unpaired; suprathreshold $n = 14/18$, subthreshold $n = 14/20$; right: paired; $n = 9/10$). **c**, Same as **a** and **b** for RhoA activity (left: unpaired; suprathreshold $n = 9/9$, subthreshold $n = 17/22$; right: paired; $n = 13/24$). **d**, Summary of data from **a**–**c**. Bars represent average peak activity. For unpaired conditions, the peak is the average of the first 2 min following uncaging. For paired conditions, the peak for suprathreshold spines corresponds to the first 2 min after the second stimulus; RhoA: 1–2 min after the first stimulus) to account for signal spreading. $*P < 0.05$, analysis of variance (ANOVA) with Tukey–Kramer’s post-hoc test. **e**, Top, representative two-photon images of the effect of expressing CA-Cdc42 on the spine-specificity of sLTP. Yellow arrows mark non-targeted spines that increased in intensity after uncaging at the

target (red circle) spine. The green arrow represents a new spine. Bottom, representative images of a typical sLTP experiment in which there is no heterosynaptic effect of uncaging. Image size, $12 \times 12 \mu\text{m}$. **f**, Quantification of the average change in nearby ($< \sim 5 \mu\text{m}$) spine volume after glutamate uncaging in control (black curve; $n = 13$ cells/13 targeted spines/112 neighbouring spines), CA-Cdc42-expressing (green curve; $n = 9$ cells/14 targeted spines/102 neighbouring spines), and CA-Cdc42-plus W56–mCh–MTBD-expressing (red curve; $n = 5$ cells/11 targeted spines/78 neighbouring spines) cells. **g**, Summary of data in **f**. $*P < 0.05$, ANOVA with Tukey–Kramer’s test. **h**, Proposed model. Calcium through NMDARs from a strong stimulus activates CaMKII, supporting autocrine BDNF–TrkB signalling, and conferring actin cytoskeleton remodelling through Rac1 and Cdc42. In parallel, CaMKII-dependent RhoA activation also acts on the actin cytoskeleton. The combination of the three GTPases is necessary to produce sLTP. Rac1 and RhoA activity spread out of the stimulated spine into the dendrite and surrounding spines, which is insufficient to produce sLTP. However, even a weak stimulus (red dotted line), can cause sufficient BDNF release to activate Cdc42, complementing the activity of Rac1 and RhoA and allowing synaptic crosstalk.

Consistent with the hypothesis that Rac1 activity spreading is required for synaptic crosstalk, the expression of W56–mCh–MTBD reduced crosstalk without significantly affecting sLTP (Fig. 3g). By contrast, a similar expression level of scr–mCh–MTBD affected neither sLTP nor crosstalk (Fig. 3g, Extended Data Fig. 8b). To test the specificity of this manipulation further, we tethered the Rac1-specific GTPase-activating protein ARHGAP15 (ref. 26) to MTBD. This construct also reduced Rac1 activity spreading without significantly affecting activation in the spine, and inhibited crosstalk without affecting sLTP (Extended Data Fig. 8f–k). Thus, activation of Rac1 in the dendritic shaft is necessary for synaptic crosstalk.

Since RhoA activation also spreads into nearby spines during sLTP, we next tested whether this BDNF-independent signal is also required for synaptic crosstalk. To do this, we tethered dominant-negative RhoA (DNRhoA) to mCh–MTBD (Fig. 3d). Expressing DNRhoA–mCh–MTBD significantly reduced a portion of RhoA activity spreading (Fig. 3e, f), and also blocked crosstalk without significantly affecting sLTP ($\Delta V_{\text{supra sustained}} = 66 \pm 6\%$, $\Delta V_{\text{sub sustained}} = 21 \pm 6\%$) (Fig. 3h, i). Importantly, using this same strategy against Cdc42 (the activity of

which is compartmentalized in spines) had no effect on either sLTP or crosstalk ($\Delta V_{\text{supra sustained}} = 60 \pm 7\%$, $\Delta V_{\text{sub sustained}} = 56 \pm 6\%$) (Fig. 3h, i), suggesting that this approach is only effective when targeting proteins with diffusive activation profiles. Taken together, these data suggest that the convergence of BDNF-dependent Rac1 signalling and BDNF-independent RhoA signalling at nearby spines primes these regions for facilitated structural plasticity.

To examine how crosstalk is achieved despite signal spreading conferring activation of only a subset of GTPases, we measured the activation of Rho GTPases in response to both unpaired and paired suprathreshold and subthreshold stimuli (Fig. 4a–d; see Extended Data Fig. 9a, b for response variability and Extended Data Figs 9c and 10 for volume curves of subthreshold stimuli). We found that both RhoA and Rac1, which show diffusive activity profiles, were only weakly activated by unpaired subthreshold stimuli (Fig. 4a, c). However, when paired with nearby suprathreshold stimuli, signal spreading supplied the crosstalk spines with additional Rac1 and RhoA activation (Fig. 4a, c, d). By contrast, Cdc42 was strongly activated by a subthreshold stimulus in both the unpaired and paired conditions, thus explaining how

nearby spines achieve the required levels of Cdc42 activation during crosstalk (Fig. 4b, d). Thus, through a combination of low-threshold, spine-specific Cdc42 activation and signal spreading of RhoA/Rac1 provided by nearby sLTP, Rho GTPase signalling complementation facilitates detection of weak synaptic activity proximal to sites of sLTP. Notably, a weak stimulus also caused a modest level of BDNF release (as measured by BDNF fused to the pH-sensitive fluorophore superecliptic pHluorin; BDNF-SEP) and TrkB activation, supporting the notion that this pathway is still functional during a weak stimulus (Extended Data Fig. 9d, e).

The compartmentalized nature of Cdc42 activity in spines probably serves to prevent nonspecific structural plasticity at nearby inactive synapses. Consistent with this model, stimulation of a single spine on cells expressing constitutively active (CA)-Cdc42 caused significant enlargement of surrounding, unstimulated spines ($\Delta V_{\text{nearby sustained}} = 42 \pm 11\%$) (Fig. 4e–g). This is in sharp contrast to control conditions, in which nearby spines show no average change in volume ($\Delta V_{\text{nearby sustained}} = -2 \pm 4\%$) (Fig. 4e–g). Importantly, sLTP in the stimulated spines was similar to that of control (Fig. 4e–g). Furthermore, when CA-Cdc42 was co-expressed with W56-mCh-MTBD, sLTP in nearby spines was suppressed without affecting sLTP at the stimulated spines ($\Delta V_{\text{nearby sustained}} = 3 \pm 3\%$; $\Delta V_{\text{stim sustained}} = 70 \pm 13\%$) (Fig. 4e–g), suggesting that the heterosynaptic effects imparted by CA-Cdc42 depend on Rac1 signal spreading. Thus, removing the compartmentalization of Cdc42 activation degrades the input-specificity of sLTP, likely by complementing the typical priming effects of diffusive Rac1 and RhoA signals.

Collectively, our data suggest that simultaneous activation of Rac1, Cdc42 and RhoA predicts the occurrence of sLTP, while activation of a subset of these proteins primes spines for sLTP (Fig. 4h). The activation of both Cdc42 and Rac1 required postsynaptic, autocrine BDNF, and conveyed the occurrence of sLTP over both spine-specific (Cdc42) and heterosynaptic (Rac1) domains. The spreading of BDNF-TrkB-mediated Rac1 signalling out of the stimulated spine was necessary for facilitating sLTP in nearby spines, consistent with the known proplasticity properties of BDNF^{22,27–29}. The spreading of BDNF-independent RhoA activation was also necessary for synaptic crosstalk, suggesting that both BDNF-dependent and -independent signalling pathways must be coordinated to achieve this phenomenon. The combination of spine-specific, low-threshold Cdc42 activation together with diffusive, high-threshold RhoA and Rac1 activation is perfectly positioned to simultaneously achieve both spine-specific homosynaptic sLTP and facilitation of sLTP in surrounding spines. Thus, our model, based on the coincident activation of three small GTPase molecules Rac, Rho and Cdc42, together with the autocrine BDNF signalling, provides a unified theory for both homo- and heterosynaptic plasticity.

Online Content Methods, along with any additional Extended Data display items and Source Data, are available in the online version of the paper; references unique to these sections appear only in the online paper.

Received 3 June; accepted 22 August 2016.

Published online 28 September 2016.

1. Tashiro, A., Minden, A. & Yuste, R. Regulation of dendritic spine morphology by the rho family of small GTPases: antagonistic roles of Rac and Rho. *Cereb. Cortex* **10**, 927–938 (2000).
2. Dietz, D. M. *et al.* Rac1 is essential in cocaine-induced structural plasticity of nucleus accumbens neurons. *Nat. Neurosci.* **15**, 891–896 (2012).
3. Murakoshi, H., Wang, H. & Yasuda, R. Local, persistent activation of Rho GTPases during plasticity of single dendritic spines. *Nature* **472**, 100–104 (2011).
4. Okamoto, K., Nagai, T., Miyawaki, A. & Hayashi, Y. Rapid and persistent modulation of actin dynamics regulates postsynaptic reorganization underlying bidirectional plasticity. *Nat. Neurosci.* **7**, 1104–1112 (2004).
5. Nakayama, A. Y., Harms, M. B. & Luo, L. Small GTPases Rac and Rho in the maintenance of dendritic spines and branches in hippocampal pyramidal neurons. *J. Neurosci.* **20**, 5329–5338 (2000).
6. Haditsch, U. *et al.* A central role for the small GTPase Rac1 in hippocampal plasticity and spatial learning and memory. *Mol. Cell. Neurosci.* **41**, 409–419 (2009).

7. Lai, K.-O. *et al.* TrkB phosphorylation by Cdk5 is required for activity-dependent structural plasticity and spatial memory. *Nat. Neurosci.* **15**, 1506–1515 (2012).
8. Il Hwan, K., Hong, W., Scott, H. S. & Ryohei, Y. Loss of Cdc42 leads to defects in synaptic plasticity and remote memory recall. *eLife* **3**, e02839 (2014).
9. Machacek, M. *et al.* Coordination of Rho GTPase activities during cell protrusion. *Nature* **461**, 99–103 (2009).
10. McAllister, A. K. Biolistic transfection of neurons. *Sci. STKE* **2000**, p11 (2000).
11. Stoppini, L., Buchs, P. A. & Muller, D. A simple method for organotypic cultures of nervous tissue. *J. Neurosci. Methods* **37**, 173–182 (1991).
12. Yasuda, R. *et al.* Supersensitive Ras activation in dendrites and spines revealed by two-photon fluorescence lifetime imaging. *Nat. Neurosci.* **9**, 283–291 (2006).
13. Matsuzaki, M., Honkura, N., Ellis-Davies, G. C. & Kasai, H. Structural basis of long-term potentiation in single dendritic spines. *Nature* **429**, 761–766 (2004).
14. Honkura, N., Matsuzaki, M., Noguchi, J., Ellis-Davies, G. C. & Kasai, H. The subsynaptic organization of actin fibers regulates the structure and plasticity of dendritic spines. *Neuron* **57**, 719–729 (2008).
15. Harward, S. C. *et al.* Autocrine BDNF-TrkB signalling within a single dendritic spine. *Nature* <http://dx.doi.org/10.1038/nature19766> (2016).
16. Lu, W. *et al.* Subunit composition of synaptic AMPA receptors revealed by a single-cell genetic approach. *Neuron* **62**, 254–268 (2009).
17. Luikart, B. W. *et al.* TrkB has a cell-autonomous role in the establishment of hippocampal Schaffer collateral synapses. *J. Neurosci.* **25**, 3774–3786 (2005).
18. Miyamoto, Y., Yamauchi, J., Tanoue, A., Wu, C. & Mobley, W. C. TrkB binds and tyrosine-phosphorylates Tiam1, leading to activation of Rac1 and induction of changes in cellular morphology. *Proc. Natl Acad. Sci. USA* **103**, 10444–10449 (2006).
19. Harvey, C. D. & Svoboda, K. Locally dynamic synaptic learning rules in pyramidal neuron dendrites. *Nature* **450**, 1195–1200 (2007).
20. Harvey, C. D., Yasuda, R., Zhong, H. & Svoboda, K. The spread of Ras activity triggered by activation of a single dendritic spine. *Science* **321**, 136–140 (2008).
21. Chen, X. *et al.* A chemical-genetic approach to studying neurotrophin signaling. *Neuron* **46**, 13–21 (2005).
22. Huber, K. M., Sawtell, N. B. & Bear, M. F. Brain-derived neurotrophic factor alters the synaptic modification threshold in visual cortex. *Neuropharmacology* **37**, 571–579 (1998).
23. Gao, Y., Xing, J., Streuli, M., Leto, T. L. & Zheng, Y. Trp(56) of rac1 specifies interaction with a subset of guanine nucleotide exchange factors. *J. Biol. Chem.* **276**, 47530–47541 (2001).
24. Korobova, F. & Svitkina, T. Molecular architecture of synaptic actin cytoskeleton in hippocampal neurons reveals a mechanism of dendritic spine morphogenesis. *Mol. Biol. Cell* **21**, 165–176 (2010).
25. Zhong, H. *et al.* Subcellular dynamics of type II PKA in neurons. *Neuron* **62**, 363–374 (2009).
26. Seoh, M. L., Ng, C. H., Yong, J., Lim, L. & Leung, T. ArhGAP15, a novel human RacGAP protein with GTPase binding property. *FEBS Lett.* **539**, 131–137 (2003).
27. Tanaka, J. *et al.* Protein synthesis and neurotrophin-dependent structural plasticity of single dendritic spines. *Science* **319**, 1683–1687 (2008).
28. Korte, M. *et al.* Hippocampal long-term potentiation is impaired in mice lacking brain-derived neurotrophic factor. *Proc. Natl Acad. Sci. USA* **92**, 8856–8860 (1995).
29. Bosch, M. *et al.* Structural and molecular remodeling of dendritic spine substructures during long-term potentiation. *Neuron* **82**, 444–459 (2014).
30. He, X. P. *et al.* Conditional deletion of TrkB but not BDNF prevents epileptogenesis in the kindling model. *Neuron* **43**, 31–42 (2004).

Supplementary Information is available in the online version of the paper.

Acknowledgements This work was supported by grants from NIMH (R01MH080047 (R.Y.), R01NS068410 (R.Y.)), NINDS (F31NS078847 (S.C.H.), R01NS05621 (J.O.M.), DP1NS096787 (R.Y.)), JSPS KAKENHI (H.M.), JST PRESTO (H.M.), the Wakeman Fellowship at Duke University (S.C.H.) and Max Planck Florida Institute (R.Y.). We thank A. E. West, S. Soderling, and F. Wang for guidance and valuable discussion, and Yasuda and McNamara laboratory members for discussion. We also thank R. Puranam for isolating MTBD. Finally, we thank D. Kloetzer for managing the laboratory.

Author Contributions N.G.H., S.C.H., J.O.M. and R.Y. designed the experiments. N.G.H., S.C.H. and H.M. developed the sensor and inhibitors; N.G.H. and S.C.H. collected the data with assistance from C.E.H.; N.G.H., S.C.H., C.E.H. and R.Y. analysed the data; N.G.H., S.C.H., J.M.O. and R.Y. wrote the paper. All authors discussed the results and comments on this manuscript.

Author Information Reprints and permissions information is available at www.nature.com/reprints. The authors declare no competing financial interests. Readers are welcome to comment on the online version of the paper. Correspondence and requests for materials should be addressed to R.Y. (ryohei.yasuda@mpfi.org).

Reviewer Information *Nature* thanks B. Bingol, H. Zhang and the other anonymous reviewer(s) for their contribution to the peer review of this work.

Purified sfGFP–Rac1 was loaded with GppNHp (2;3'-*O*-*N*-methyl anthraniloyl-GppNHp) and GDP by incubating in the presence of tenfold molar excess of GppNHp and GDP in MgCl₂-free PBS containing 1 mM EDTA for 10 min, respectively. The reaction was terminated by adding 10 mM MgCl₂. sfGFP–Rac1 and mCh–PDB2 were mixed and incubated at room temperature for 20 min. FRET between sfGFP and mCh was measured under 2pFLIM, and the fraction of sfGFP–Rac1 bound to mCh–PDB2 was calculated by fitting the fluorescence lifetime curve with a double exponential function (equation (1)). The dissociation constant was obtained by fitting the relationship between the binding fraction and the concentration of mCh–PDB2 ([mCh–PDB2]) with a Michaelis–Menten function.

Statistical methods. Sample sizes for all experiments were chosen based on signal-to-noise ratios identified in pilot experiments.

The variances of all data were estimated and compared using Bartlett's test or Levene's test before further statistical analysis.

The distribution patterns of Rho GTPase sensor activity was determined by performing a Shapiro–Wilk test for normality on the peak response (the same points used for statistical comparisons). All of the sensors tested adhered to the null hypothesis, and thus are considered normally distributed. As such, parametric statistics were used to compare values of Rho GTPases response.

For multiple comparisons of sensor activity, data were first subjected to ANOVA, followed by a post-hoc test to determine statistical significance, according to the structure of the comparison being made. In cases where each condition is being compared to all other conditions in the group, the Tukey–Kramer method was used. In cases where each condition is being compared to a single control, Dunnett's test was used instead.

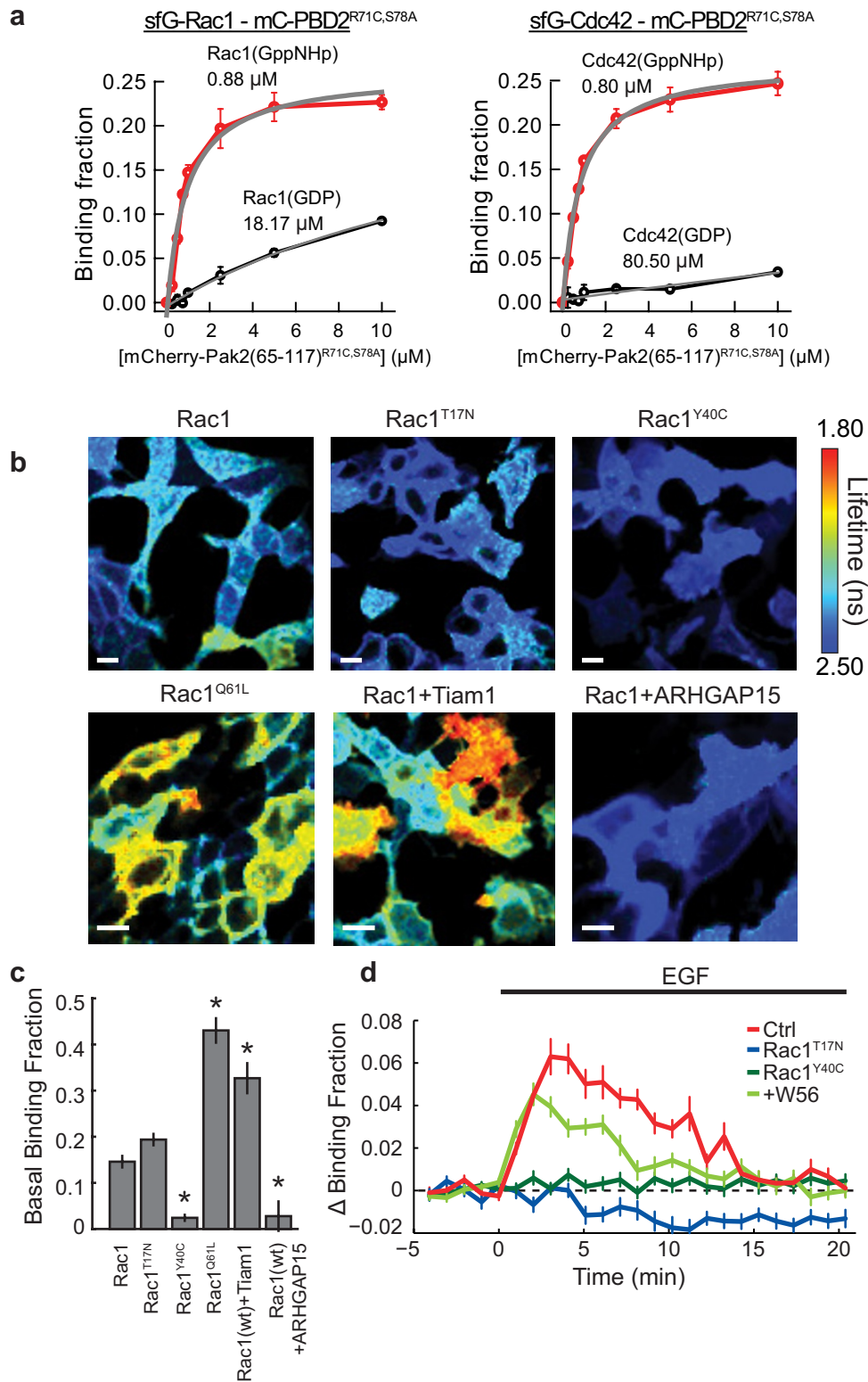
To compare values of non-normally distribution changes in spine volume, data were log-transformed to resolve skewness, then subjected to normal parametric

statistics, as indicated in the figure legends. To support these statistical claims, non-parametric statistics were also applied to the original, non-transformed data using a Wilcoxon rank-sum test in place of *t*-tests, and the Kruskal–Wallis procedure in place of ANOVA, followed by a post-hoc analysis using Dunn's test. All of the data tested were significant by both of these approaches.

Data were only excluded if obvious signs of poor cellular health (for example, dendritic blebbing, spine collapse) were apparent.

Crosstalk experiments comparing different genetic perturbations were performed in a blinded fashion. Experimenters were unblinded when either statistical significance was reached, or when experimental number was comparable to similar experiments that had reached statistical significance.

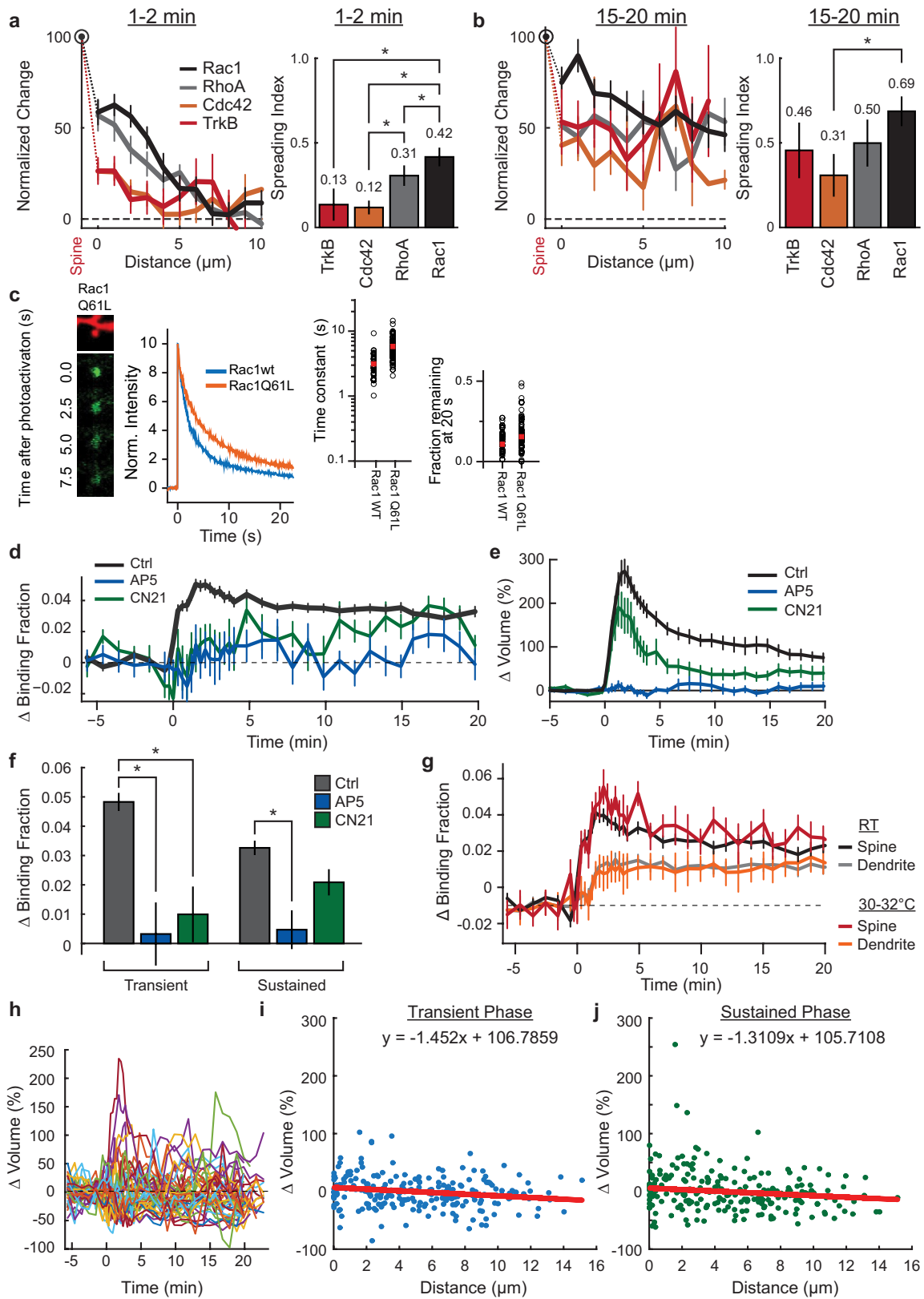
30. Chrostek, A. *et al.* Rac1 is crucial for hair follicle integrity but is not essential for maintenance of the epidermis. *Mol. Cell. Biol.* **26**, 6957–6970 (2006).
31. Yasuda, R. Imaging spatiotemporal dynamics of neuronal signaling using fluorescence resonance energy transfer and fluorescence lifetime imaging microscopy. *Curr. Opin. Neurobiol.* **16**, 551–561 (2006).
32. Murakoshi, H., Lee, S.-J. & Yasuda, R. Highly sensitive and quantitative FRET-FLIM imaging in single dendritic spines using improved non-radiative YFP. *Brain Cell Biol.* **36**, 31–42 (2008).
33. Pologruto, T. A., Sabatini, B. L. & Svoboda, K. ScanImage: flexible software for operating laser scanning microscopes. *Biomed. Eng. Online* **2**, 13 (2003).
34. Shaner, N. C. *et al.* Improved monomeric red, orange and yellow fluorescent proteins derived from *Discosoma* sp. red fluorescent protein. *Nat. Biotech.* **22**, 1567–1572 (2004).
35. Pédelacq, J. D., Cabantous, S., Tran, T. & Terwilliger, T. C. Engineering and characterization of a superfolder green fluorescent protein. *Nat. Biotech.* **24**, 79–88 (2005).



Extended Data Figure 1 | See next page for caption.

Extended Data Figure 1 | Design and characterization of the Rac1 sensor. **a**, Measurements of the affinity between sfGFP–Rac1 or sfGFP–Cdc42 and the p21-activated-kinase-derived acceptor construct, PAK2(65–117)^{R71C,S78A}. The binding fraction was measured using 2pFLIM (see Methods) across several concentrations of the acceptor construct. The dissociation constant was obtained by fitting the data (red) with a Michaelis–Menten function (grey). **b**, Representative fluorescence lifetime images of Rac1 sensor variants in HEK293T cells. Cells were transfected with a 1:2 donor:acceptor ratio of wild-type, dominant-negative (Rac1^{T17N}), substrate-binding dead (Rac1^{Y40C}), or constitutively active (Rac1^{Q61L}) variants of Rac1 with mCh–PBD2^{R71C,S78A}–mCh. Some experiments included the addition of an additional construct (the Rac1 guanine nucleotide exchange factor (GEF) Tiam1, or GTPase-activating protein (GAP) ARHGAP15) in a 1:2:1 donor:acceptor:GEF/GAP ratio. Cells were imaged 12–36 h after transfection in a warmed solution containing 30 mM Na-HEPES, pH 7.3, 130 mM NaCl, 2.5 mM KCl, 1 mM

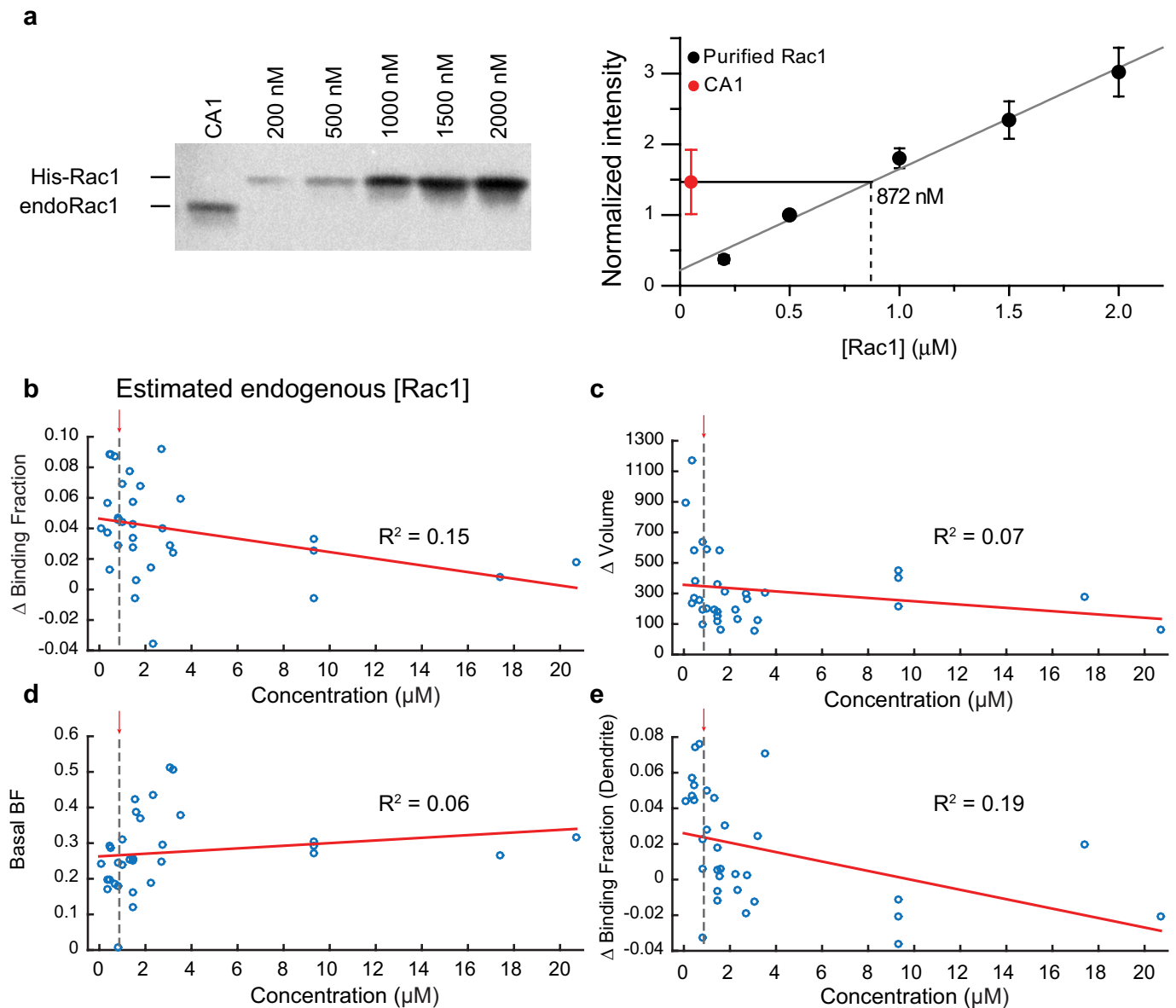
CaCl₂, 1 mM MgCl₂, 2 mM NaHCO₃, 1.25 mM NaH₂PO₄ and 25 mM glucose. Warmer colours indicate a lower fluorescence lifetime value/higher binding fraction of eGFP–Rac1 to the acceptor construct. Scale bars, 50 μm. **c**, Basal binding fraction of Rac1–PBD2^{R71C,S78A} for the conditions listed in **b**. Error bars represent s.e.m. **P* < 0.0001 compared to wild-type Rac1 control condition, ANOVA followed by post-hoc tests using the least significant difference. **d**, Time course of Rac1 activation in HEK293T cells upon application of 100 μg ml⁻¹ epidermal growth factor (EGF). Control experiment corresponds to eGFP–Rac1 (donor) plus mCh–PBD2^{R71C,S78A}–mCh (acceptor) expression alone (*n* = 39 cells/8 plates), Rac1^{T17N} (*n* = 33 cells/4 plates) and Rac1^{Y40C} (*n* = 40 cells/5 plates) corresponds to the expression of the donor variant with the acceptor in the same ratio as controls, and Rac1 plus W56 corresponds to the expression of the wild-type donor with the acceptor and the Rac1 inhibitory peptide W56.



Extended Data Figure 2 | See next page for caption.

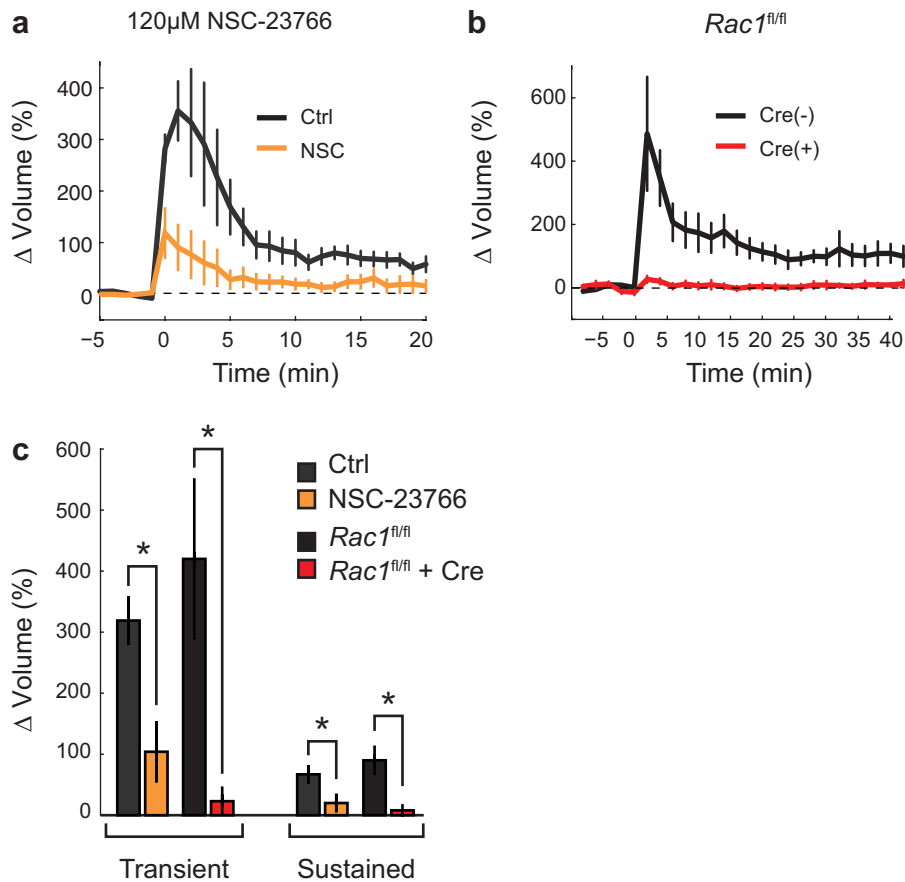
Extended Data Figure 2 | Characterization of the Rac1 sensor during single spine structural plasticity in hippocampal slices. **a**, Left, comparison of the signal spreading of Rac1, RhoA, Cdc42 and TrkB, normalized to spine activity from 1–2 min after stimulus onset. Error bars represent s.e.m. Data correspond to that shown in Fig. 1. Right, comparison of the spreading indices of the four sensors (spreading index = activity in dendrite (1–5 μm) from 1–2 min post-stimulation/maximum spine activation). Error was estimated by bootstrapping. * $P < 0.05$, independent-samples t -test. **b**, Same as **a**, but for 15–20 min after stimulation. **c**, Analysis of the diffusion time constants of constitutively active (Q61L) and wild-type Rac1 using photo-activatable GFP (paGFP). Left, representative 2p images of paGFP–Rac1^{Q61L} in a single dendritic spine after photo-activation. While active Rac1 shows a slightly slower diffusion than wild-type Rac1 (middle), both Rac1^{Q61L} and wild-type Rac1 diffuse away from the spine within approximately 10 s, similarly to Cdc42 and RhoA (ref. 3) (right two plots; wild type: $n = 41$ spines/4 cells; Rac1^{Q61L}: 67 spines/7 cells). **d**, Pharmacological characterization of Rac1 signal during sLTP. Rac1 activation in control ($n = 102$ cells/121 spines) conditions during 2p-glutamate uncaging, in the presence of the NMDAR blocker APV (100 μM ; $n = 6$ cells/13 spines), and in the presence of the cell-permeable CaMKII inhibitory peptide tatCN21 (CN21; 10 μM ; $n = 5$ cells/11 spines). Error bars represent s.e.m. **e**, Time course of spine volume change for experiments (**d**). Error bars

represent s.e.m. **f**, Summary of effect of AP5 and CN21 on the transient (1–2 min after stimulation; control = 0.049 ± 0.003 ; AP5 = 0.00 ± 0.01 ; CN21 = 0.01 ± 0.01) and sustained (>10 min after stimulation; control = 0.033 ± 0.002 ; AP5 = 0.006 ± 0.007 ; CN21 = 0.026 ± 0.05) phases of Rac1 activation during sLTP. Error bars represent s.e.m. * $P < 0.05$, independent-samples t -test. **g**, Effects of near-physiological temperature of Rac1 sensor activation. Perfusion was warmed with a heating block holding the ACSF container, and the temperature measured at the back of the perfusion chamber (room temperature (RT), $n = 102$ cells/121 spines; for 30–32 $^{\circ}\text{C}$, $n = 11$ cells/13 spines). Error bars represent s.e.m. **h**, Variability of unstimulated spine volume changes after the induction of sLTP in a nearby spine in Rac1 sensor-overexpressing neurons. Data shown are time courses of unstimulated spines close to the site of sLTP induction. While there is no average change in nearby spine volume with this stimulus (Fig. 1c), there is occasional enlargement or shrinkage. Data correspond to 100 randomly selected spines from the total of 777 nearby spines measured for the average depicted in Fig. 1c. **i**, Transient (1–2 min) change in volume of nearby spines as a function of distance from the stimulated spine. Data correspond to all nearby spines measured for the experiments in which the spatial profile of Rac1 was measured ($n = 56$ cells/79 experiments/218 nearby spines; Fig. 1e). Inset equation corresponds to the linear model of best fit. **j**, Same as **i**, but for the sustained (10–20 min) change in volume of nearby spines.



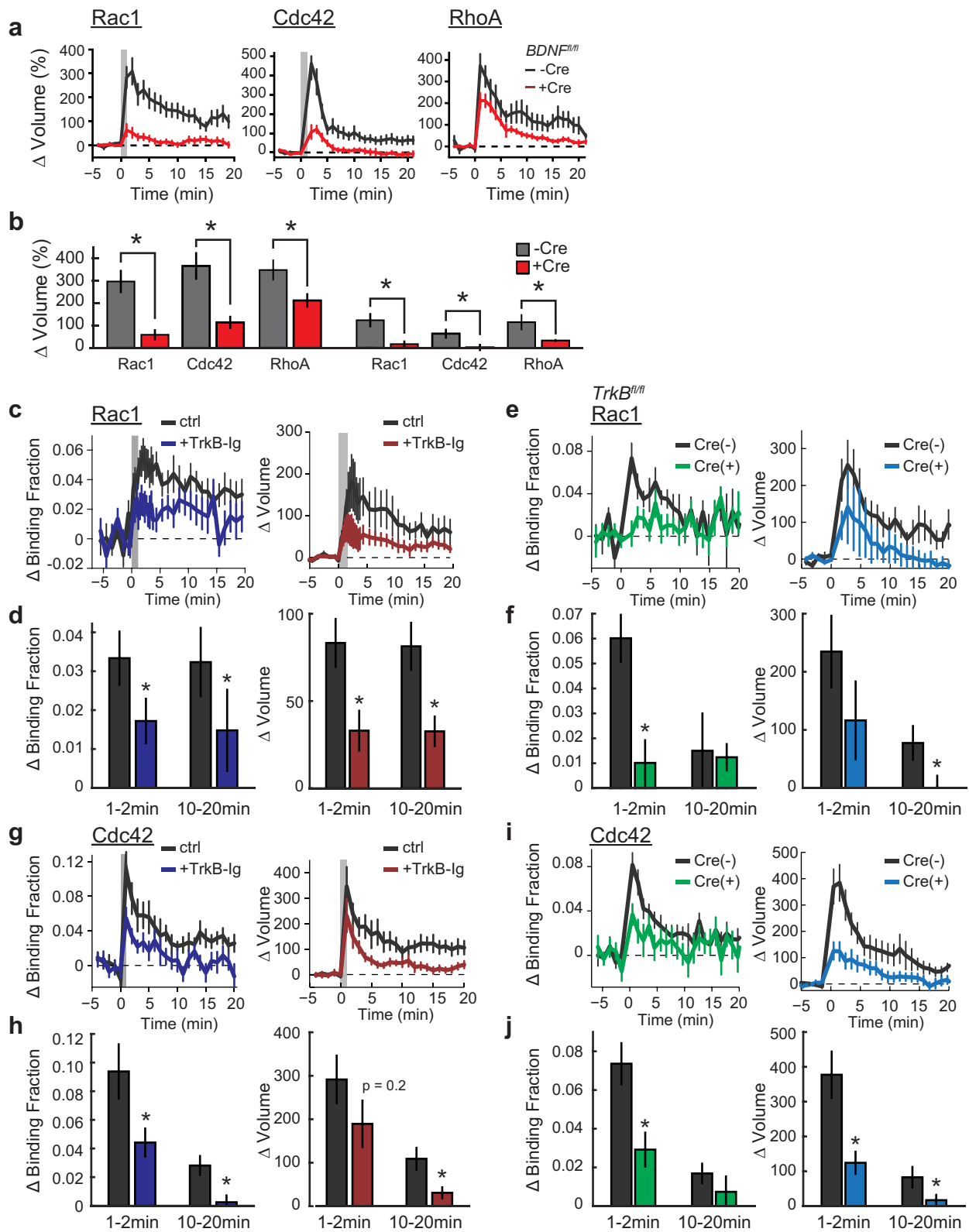
Extended Data Figure 3 | Estimation of endogenous Rac1 concentration and effects of Rac1 sensor overexpression. **a**, Left, representative western blot used to analyse endogenous Rac1 expression (endo-Rac1) from the CA1 region of hippocampal slices cultures compared to known concentrations of purified polyhistidine-tagged Rac1 (His-Rac1). Right, quantification of protein expression level for His-Rac1 from western blot shown in **a** averaged over three experiments. The concentration of endogenous Rac1 was estimated by measuring the intersection of the intensity of Rac1 protein

from CA1 on the established calibration curve. **b–e**, Effect of concentration of the Rac1 sensor on the observed change in binding fraction or volume of the spine with glutamate uncaging (**b** or **c**, respectively), the basal binding fraction of the sensor (**d**), or the change in binding fraction in the dendrite in response to uncaging (**e**). Rac1 sensor concentration was estimated by making a standard curve of the intensity values known concentrations of eGFP at a range of imaging powers. The estimated endo-Rac1 concentration is plotted with a dashed line for comparison.



Extended Data Figure 4 | Effect of Rac1 inhibition on sLTP. **a**, The effect of a high concentration of NSC-23766 (120 μ M) on uncaging-evoked spine volume change. Experiments were performed in eGFP-expressing rat hippocampal CA1 pyramidal neurons. Error bars represent s.e.m. $n = 5$ cells/9 control spines; $n = 5$ cells/15 NSC-23766 spines. **b**, Effect of single-cell Rac1 knockout on spine sLTP. *Rac1^{fl/fl}* slices were transfected with either eGFP alone (Cre (-); black curve, $n = 5$ cells/5 spines) or eGFP + tdTomato-Cre recombinase (Cre (+); red curve; $n = 7$ cells/

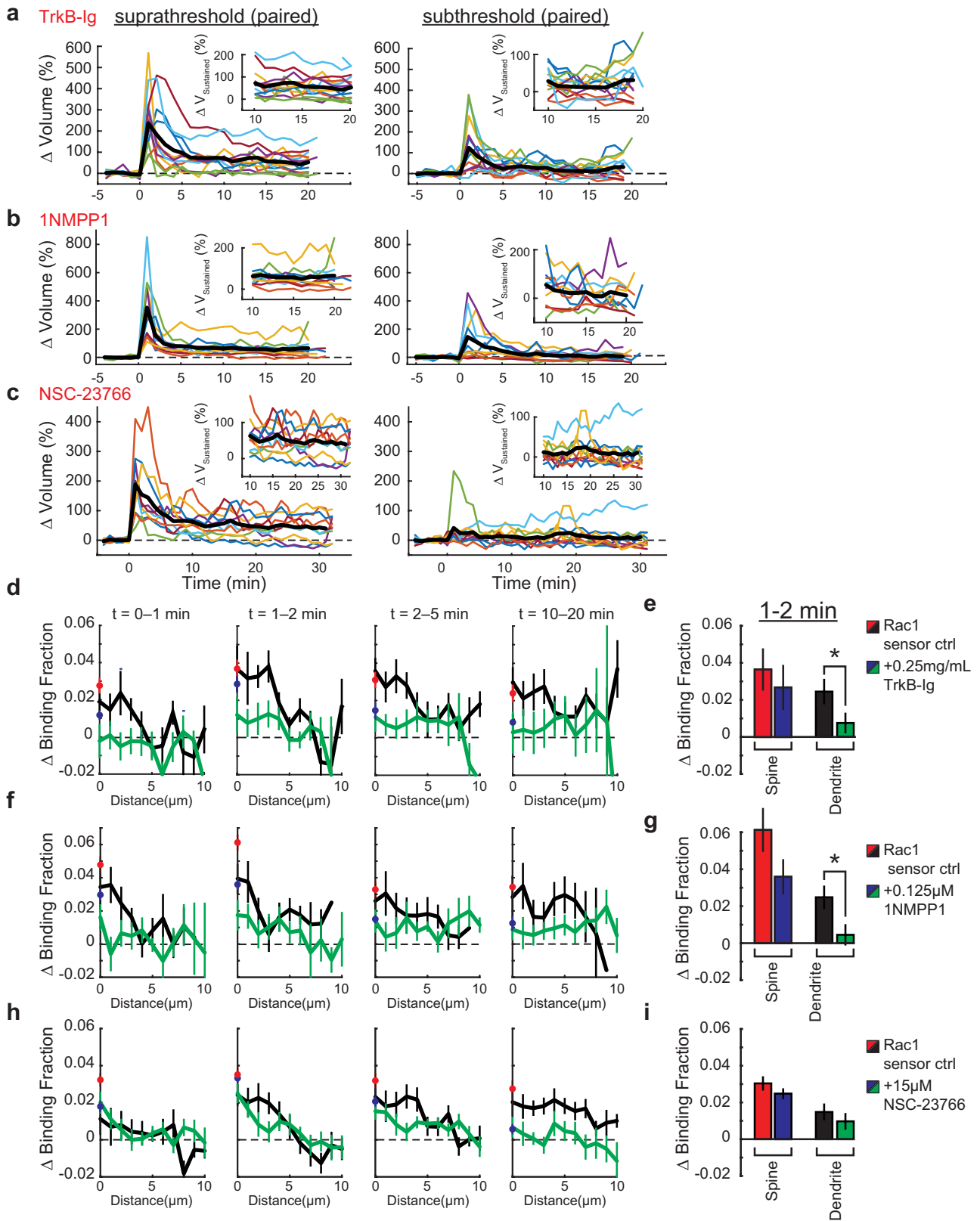
7 spines). Error bars represent s.e.m. **c**, Summary of data in **a** and **b**. For NSC-23766 experiments, control $\Delta V_{\text{transient}} = 319 \pm 38\%$; control $\Delta V_{\text{sustained}} = 67 \pm 13\%$; NSC-23766 $\Delta V_{\text{transient}} = 104 \pm 48\%$; NSC-23766 $\Delta V_{\text{sustained}} = 20 \pm 13\%$. For Rac1 knockout experiments, Cre(-) $\Delta V_{\text{transient}} = 420 \pm 130\%$; Cre(-) $\Delta V_{\text{sustained}} = 90 \pm 22\%$; Cre(+) $\Delta V_{\text{transient}} = 23 \pm 9\%$; Cre(+) $\Delta V_{\text{sustained}} = 8 \pm 8\%$. Error bars represent s.e.m. * $P < 0.05$, independent-samples t -test. All data are mean \pm s.e.m.



Extended Data Figure 5 | See next page for caption.

Extended Data Figure 5 | Characterization of Rho-GTPase dependence on BDNF-TrkB signalling. **a, b**, Dependence of sLTP (Δ volume) in Rho GTPase sensor-expressing neurons on postsynaptic BDNF. Data correspond to the volume data from experiments shown in Fig. 1f. Black denotes Cre⁻, red denotes Cre⁺. **b**, Summary of data from **a**. Bars represent the average spine volume change from 10 min after stimulation to the end of the experiment. **c, d**, Dependence of Rac1 on extracellular BDNF. **c**, Left, Rac1 (ctrl: $n = 7$ cells/11 spines; TrkB-Ig: $n = 8$ cells/14 spines), activity in the presence of 2 mg ml^{-1} TrkB-Ig. Right, spine volume change in Rac1 sensor-overexpressing cells in the two conditions. Grey bars indicate duration of uncaging bout. **d**, Summary of data in **c**. **e, f**, Dependence of Rac1 on postsynaptic TrkB. **e**, Left, Rac1 (Cre(-): $n = 3$ cells/8 spines; Cre(+): $n = 3$ cells/8 spines), activity in the presence or absence of Cre recombinase in *Trkb^{fl/fl}* mouse slices. Right, spine

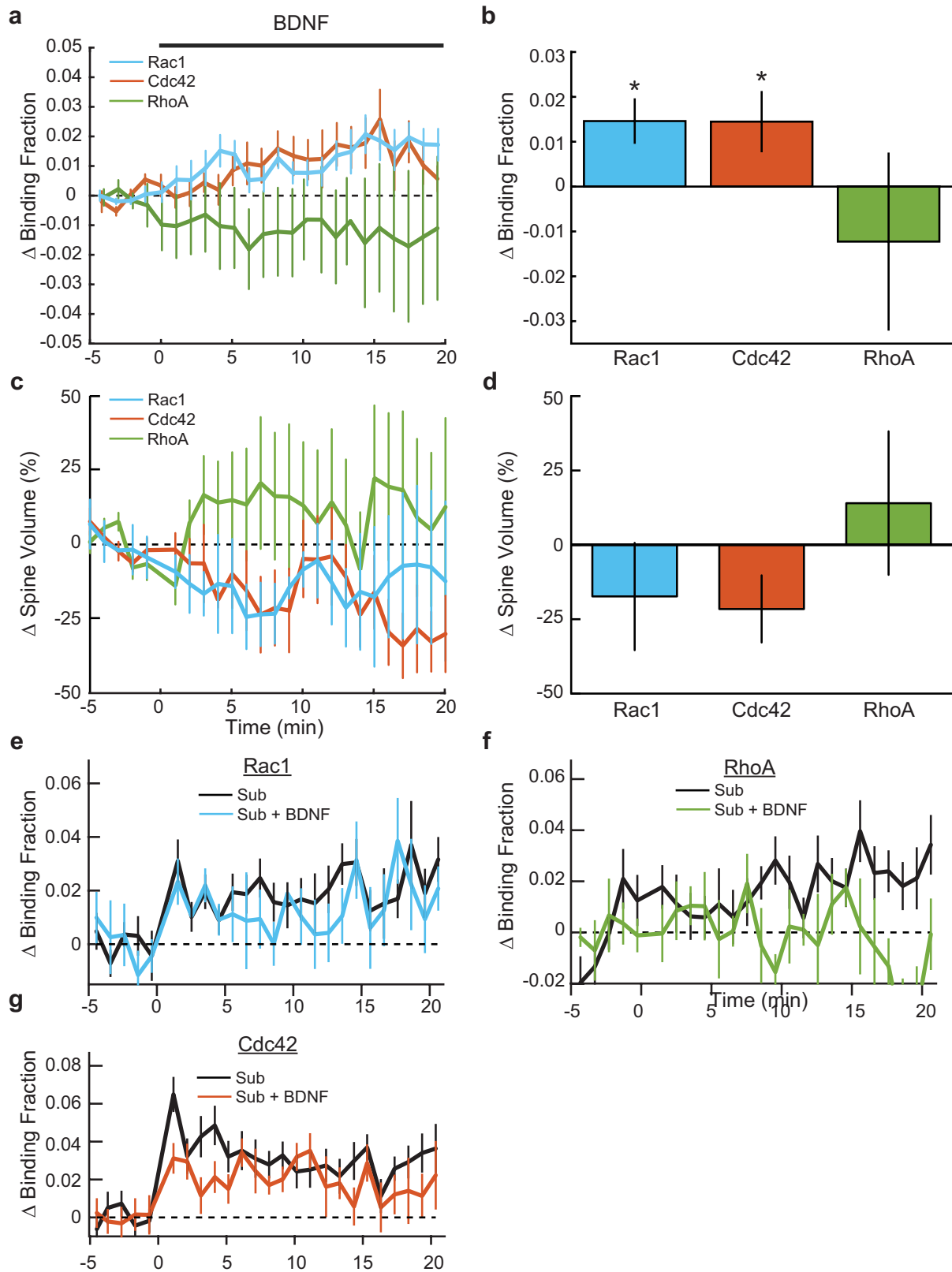
volume change in Rac1 sensor-overexpressing cells in the two conditions. Grey bars indicate duration of uncaging bout. **f**, Summary of data in **e**. **g, h**, Dependence of Cdc42 on extracellular BDNF. Left, Cdc42 ($n = 7$ cells/12 spines, 5 cells, 12 TrkB-Ig spines), activity in the presence of 2 mg ml^{-1} TrkB-Ig. Right, spine volume change in Rac1 sensor-overexpressing cells in the two conditions. Grey bars indicate duration of uncaging bout. **h**, Summary of data in **g**. **i, j**, Dependence of Cdc42 on postsynaptic TrkB. **i**, Left, Cdc42 (Cre(-): $n = 5$ cells/12 spines; Cre(+): $n = 6$ cells/16 spines), activity in the presence or absence of Cre recombinase in *Trkb^{fl/fl}* mouse slices. Right, spine volume change in Cdc42 sensor-overexpressing cells in the two conditions. Grey bars indicate duration of uncaging bout. **j**, Summary of data in **i**. All data are mean \pm s.e.m. * $P < 0.05$, two-tailed independent-samples *t*-test.



Extended Data Figure 6 | See next page for caption.

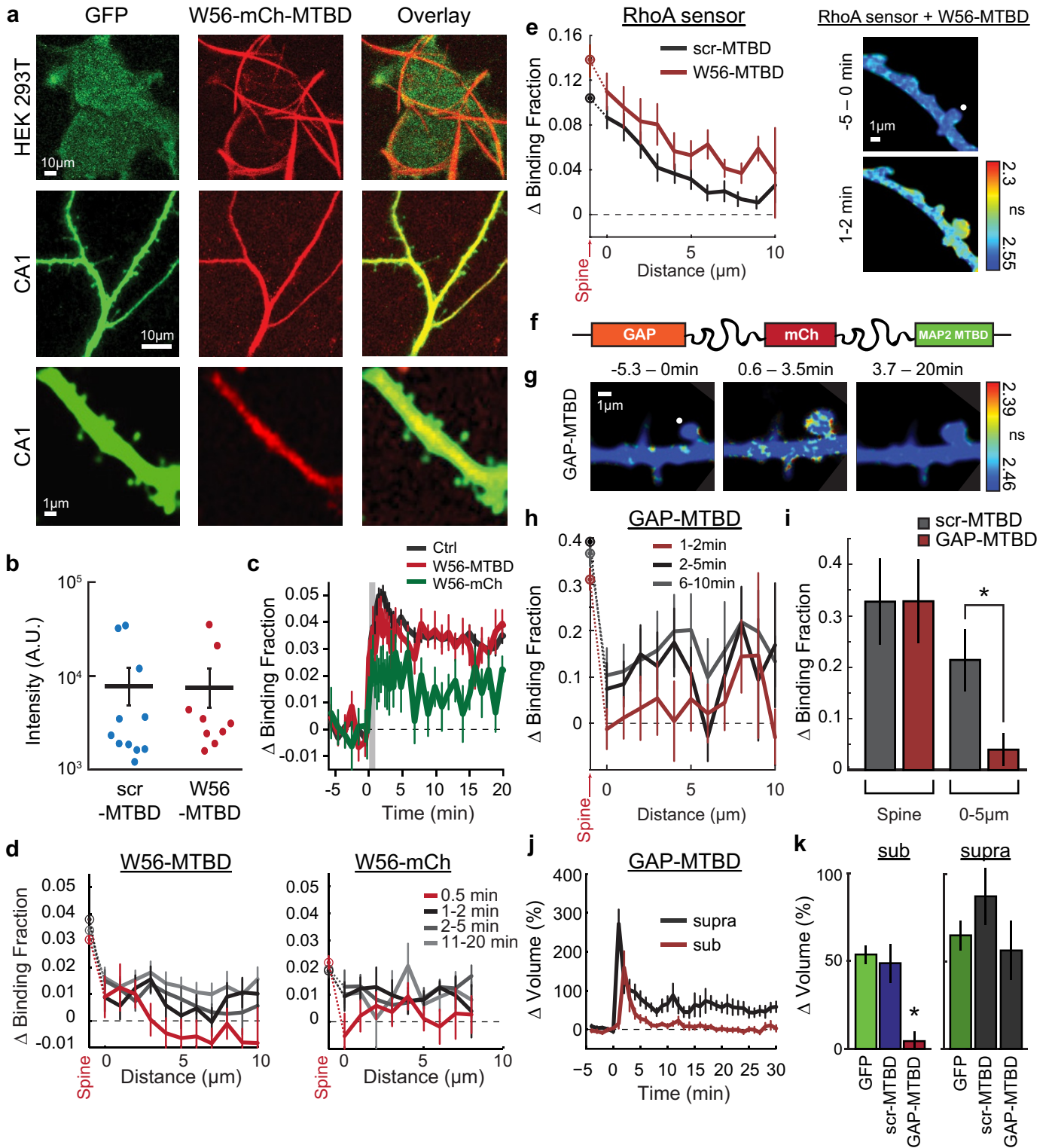
Extended Data Figure 6 | Characterization of the effects of weak pharmacological inhibition of BDNF–TrkB signalling on sLTP and Rac1 activity spreading. **a**, Individual data points for crosstalk experiments under low [TrkB-Ig] exposure. Each plot contains the average values of the experiments (thick, black curve) along with the corresponding individual experiments for the suprathreshold spine (left) and the subthreshold spine (right). Inset figures correspond to a close-up view of the data distributions for >10 min (the values used to calculate the sustained volume changes shown in Fig. 2). **b**, Same as **a**, but for crosstalk experiments using low [1NMPP1]. **c**, Same as **a** and **b**, but for crosstalk experiments using low [NSC-23766]. **d**, Effect of $0.125 \mu\text{g ml}^{-1}$ TrkB-Ig on Rac1 signal spreading. Each plot represents a specific time epoch after glutamate uncaging onset. Curves represent control (red = spine;

black = dendrite) and +TrkB-Ig (blue = spine; green = dendrite) conditions plotted as a function of distance from the stimulated spine ($n = 5$ cells/6 control spines; $n = 5$ cells/9 +TrkB-Ig spines). **e**, Summary of data in **d**. Bars represent averages of the indicated temporal window across 1–5 μm of the dendrite. **f**, Same as **d**, but with the absence (red/black) and presence (blue/green) of $0.125 \mu\text{M}$ 1NMPP1 in *TrkB^{F616A}* slices (control: $n = 5$ cells/8 spines; +1NMPP1: $n = 5$ cells/11 spines). **g**, Summary of data in **f**. Bars represent averages of the indicated temporal window across 1–5 μm of the dendrite. **h**, Same as **d** and **f**, but in the absence (red/black) and presence (blue/green) of the Rac1 inhibitor, $15 \mu\text{M}$ NSC-23766 (control: $n = 6$ cells/8 spines; NSC-23766: $n = 8$ cells/13 spines). **i**, Summary of data in **h**. Bars represent averages of the indicated temporal window across 1–5 μm of the dendrite. * $P < 0.05$, *t*-test.



Extended Data Figure 7 | Effect of BDNF application on Rho GTPase signalling. **a**, Effect of bath application of 20 ng ml^{-1} exogenous BDNF on Rac1 ($n = 8$ cells), Cdc42 ($n = 10$ cells), and RhoA ($n = 5$ cells) sensors. $*P < 0.05$, statistically different from zero, one-sample t -test. **b**, Summary of data in **a**. **c**, Effects of BDNF application on spine volume in Rac1 (blue), Cdc42 (orange), and RhoA (green) sensor-expressing cells. Data are from the experiments in **a** and **b**. **d**, Summary of data in **c**. ANOVA determined

that there was no significant difference between the sensor conditions. None of the conditions showed a significant difference from zero as determined by a one-sample t -test. **e**, Response of Rac1 to a subthreshold stimulus in the presence of 20 ng ml^{-1} BDNF (control $n = 15$ cells/15 spines; +BDNF $n = 6$ cells/6 spines) **f**, Same as **e**, but for RhoA (control $n = 14$ cells/18 spines; +BDNF $n = 7$ cells/8 spines) **g**, Same as **e** and **f**, but for Cdc42 (control $n = 17$ cells/20 spines; +BDNF $n = 7$ cells/7 spines).

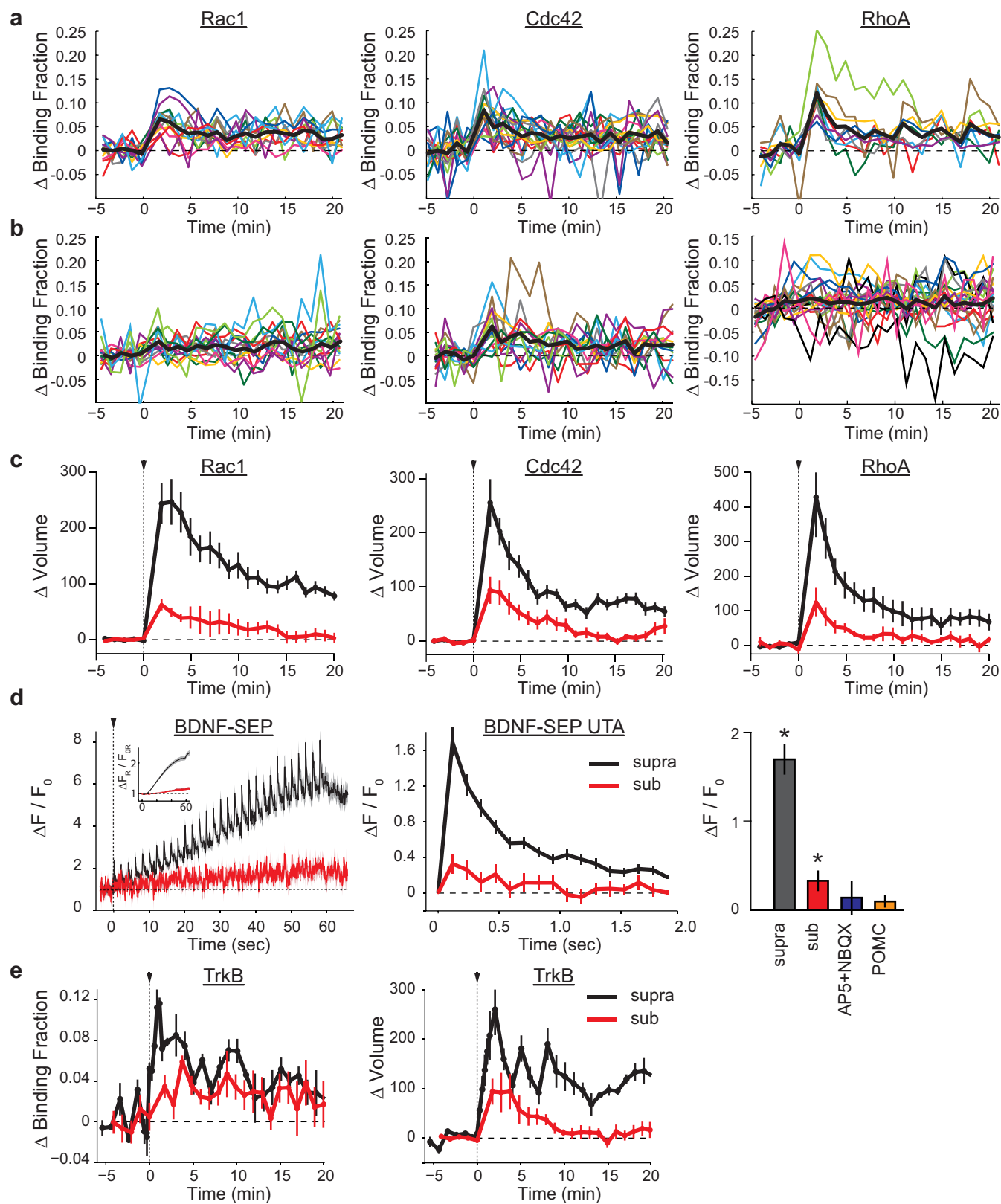


Extended Data Figure 8 | See next page for caption.

Extended Data Figure 8 | Characterization of the dendritic Rac1 inhibitor approach.

a, Representative two-photon images illustrating the filamentous distribution HEK293T cells (top row), consistent with microtubule localization, and the largely dendrite-specific localization in CA1 neurons (bottom two rows) of W56-mCh-MTBD in comparison to an eGFP cell fill (first column). HEK293T cells were imaged at 1,050 nm to increase specificity of excitation for mCh versus eGFP. All images were acquired 2–5 days after transfection. **b**, Comparison of the expression levels of scr-MTBD and W56-MTBD from a subset of cells used for synaptic crosstalk experiments. Expression was estimated by acquiring intensity values in the red channel of an $\sim 10\ \mu\text{m}$ section of a secondary dendrite using ImageJ. Each point represents a single cell. **c**, Average time course of Rac1 activation for cells expressing only the Rac1 sensor (control, black curve; $n = 105$ spines), the Rac1 sensor plus W56-mCh-MTBD (red curve; $n = 21$ cells/33 spines), and the Rac1 sensor plus W56-mC (green curve; $n = 6$ cells/13 spines). Error bars represent s.e.m. **d**, Comparison of the effect of W56-mCh-MTBD (left; $n = 21$ cells/33 spines) to untargeted W56-mCh (right; $n = 6$ cells/13 spines) on the spatial profile of Rac1 activation. Data are mean \pm s.e.m. Control corresponds to the data in Fig. 1d. **e**, Effect of expression of W56-mCh-

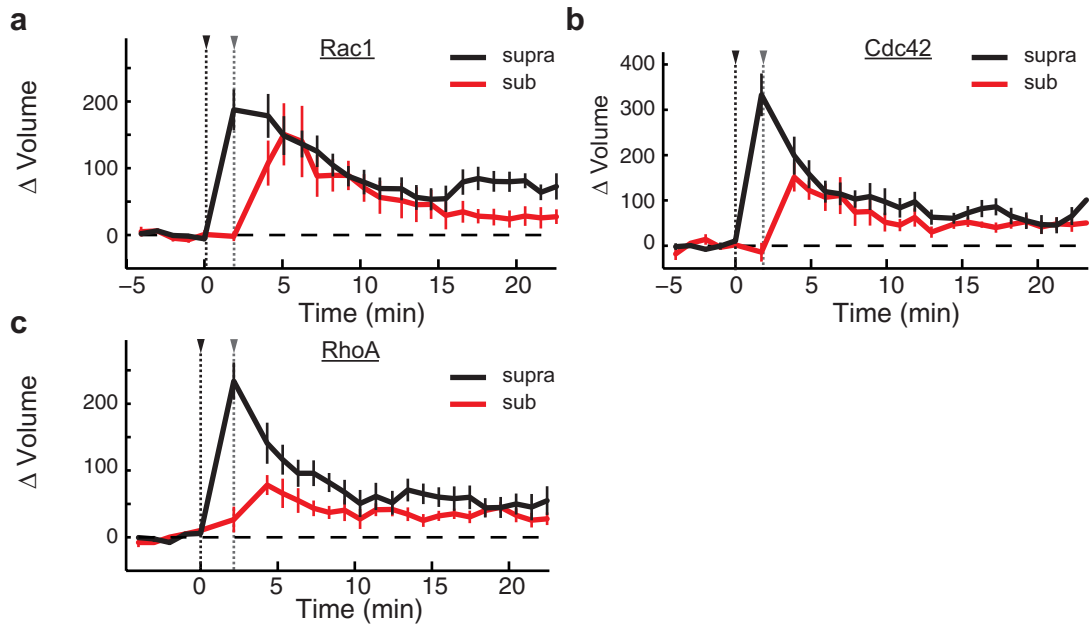
MTBD on RhoA sensor activation. Left, spatial profile of RhoA activation during sTLP induction in the presence of scr-mCh-MTBD control (black curve) and W56-mCh-MTBD (red curve). Right, representative 2pFLIM images of RhoA activation in the presence of W56-mCh-MTBD. White circle indicates the targeted spine. **f**, Schematic of the design of the GAP-based Rac1 dendritic inhibitor. A Rac1-specific GTPase-activating protein (ARHGAP15) replaced W56 in the general dendritic inhibitor construct (see Fig. 3a). **g**, Representative 2pFLIM images of the effect of GAP-mCh-MTBD on Rac1 signal spreading for the indicated time windows. White circle indicates the targeted spine. **h**, Quantification of the effects of expression of GAP-mCh-MTBD on Rac1 signal spreading after glutamate uncaging. Data are depicted as the change in binding fraction in the dendrite as a function of distance from the stimulated spine (change in binding fraction in spine plotted on y axis) ($n = 8$ cells/11 spines). **i**, Summary of the data depicted in **g** and **h**. Also shown are data for Rac1 spreading from scr-MTBD (see Fig. 3d) for comparison. $*P < 0.05$, independent-samples t -test. **j**, Effects of GAP-mCh-MTBD expression on synaptic crosstalk ($n = 4$ cells/8 crosstalk experiments). **k**, Summary of the data in **j**. $*P < 0.05$, ANOVA and post-hoc test using the Tukey-Kramer method.



Extended Data Figure 9 | See next page for caption.

Extended Data Figure 9 | Effect of a subthreshold stimulus on single spines of sensor-expressing CA1 neurons. **a**, Plots showing the variability of the response of the Rac1 (left), Cdc42 (middle), and RhoA (right) sensors to a suprathreshold stimulus. Thick black curves correspond to the averages depicted in Fig. 4a–c ('unpaired' condition) of the main text. The peak responses (1–2 min after stimulation, the same points used for statistical claims in Fig. 4) were subjected to a Shapiro–Wilk test to confirm the normality of the data. All data supported the null hypothesis, illustrating that the data are Gaussian distributed and justifying the use of parametric statistics. **b**, Plots showing the variability of the response of the Rac1 (left), Cdc42 (middle) and RhoA (right) sensors to a subthreshold stimulus. Thick black curves correspond to the averages depicted in Fig. 4a–c ('unpaired' condition). **b**, Change in spine volume with glutamate uncaging (arrow and dotted line) during an unpaired threshold (black) and subthreshold (red) stimuli for CA1 pyramidal cells expressing the Rac1 (left), Cdc42 (centre), or RhoA (right) sensors. Shaded region represents s.e.m. Data correspond to the volume curves for the data presented in Fig. 4. **c**, 8-Hz two-photon imaging of BDNF–SEP intensity

during an unpaired suprathreshold (black) or subthreshold (red) stimulus. Left, the full time course. Glutamate uncaging stimuli are delivered at 0.5 Hz beginning at $t = 0$, indicated by the black arrow and dashed line. Inset shows the associated volume change (as measured from mCh cell fill) of the two conditions. Middle panel, the uncaging-triggered average of 30 16-frame bins (corresponding to each uncaging pulse) and thus shows the average response to individual glutamate uncaging events. Right panel, the average of the first point after uncaging for the indicated conditions. Both suprathreshold and subthreshold conditions show a statistically significant difference from zero, while the presence of AP5 plus NBQX or the POMC peptide eliminate this signal. Error bars represent s.e.m. ($n = 28$ cells/217 spines (LTP), 5/84 (Sub), 2/46 AP5+NBQX), and 2/29 (POMC)). **d**, Left, activation of the TrkB sensor in response to an unpaired suprathreshold (black; $n = 4$ cells/5 spines) or subthreshold (red; $n = 6$ cells/8 spines) stimulus. Right, change in spine volume in a cell expressing the TrkB sensor in response to an unpaired threshold or subthreshold stimulus. Error bars represent s.e.m.



Extended Data Figure 10 | Change in volume of paired spines during synaptic crosstalk in Rho GTPase-expressing CA1 neurons. **a**, Spine volume change in response to a suprathreshold (black curve; black arrow indicates stimulus initiation) and a paired subthreshold (red curve, grey arrow indicates stimulus initiation) stimulus in spines from

cells expressing the Rac1 sensor ($n = 6$ cells/12 spine pairs). Error bars represent s.e.m. **b**, Same as **a**, but for Cdc42-expressing cells ($n = 9$ cells/10 spine pairs). **c**, Same as **a** and **b**, but for RhoA-expressing cells ($n = 8$ cells/12 spine pairs).